ENGINEERING Environment
2027, 21(2): 27 https://doi.org/10.1007/s11783-027-2327-9

RESEARCH ARTICLE

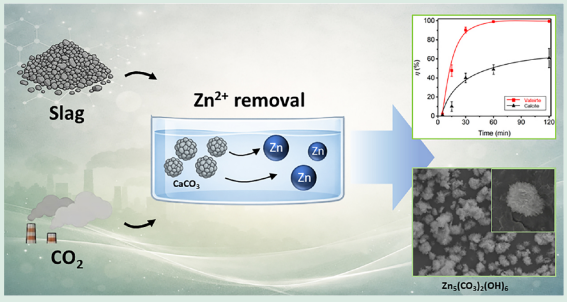
CO_2 mineralization of steel slag into vaterite for high-efficiency Zn^{2+} removal and upcycling into hydrozincite

Jaemin Park, Hyunsoo Han, Sangmin Jeon ✉

Department of Chemical Engineering, Pohang University of Science and Technology (POSTECH), 77 Cheongam-Ro, Pohang, Gyeongbuk 37673, Republic of Korea

HIGHLIGHTS

- Vaterite and calcite were synthesized via CO_2 mineralization of steel slag.
- Zn^{2+} removal efficiency was higher with vaterite than with calcite.
- Vaterite was converted into hydrozincite during Zn^{2+} adsorption.
- Time-dependent evolution confirmed hydrozincite via dissolution-reprecipitation.



ABSTRACT: We developed an integrated strategy that simultaneously valorizes three major by-products of the steel industry, including CO_2, steelmaking slag, and Zn^{2+}-containing wastewater. CO_2 mineralization was achieved by bubbling CO_2 into steel-slag leachate in the presence of amino acid crystallization modifiers, which selectively yielded the metastable $CaCO_3$ polymorph vaterite with *L*-arginine and the thermodynamically stable polymorph calcite with *L*-lysine. The resulting $CaCO_3$ was used for Zn^{2+} removal from aqueous media, where vaterite exhibited a high removal capacity of 633 mg/g, significantly higher than that of calcite (444 mg/g). Notably, Zn^{2+} removal by vaterite is governed not by simple surface adsorption but by a dissolution-reprecipitation mechanism, leading to an *in situ* transformation into Zn-rich hydrozincite. This study provides a potential pathway for CO_2 mineralization and Zn^{2+} removal while enabling the stabilization and recovery of Zn in a solid mineral form, offering a new strategy for waste to resource conversion in steel-related industries.

KEYWORDS: Steel industry, Vaterite, calcite, Zn^{2+} removal, Hydrozincite

1 Introduction

The steel industry is a major contributor to environmental impacts due to massive CO_2 emissions (Kim et al., 2022), large amounts of slag (Ibrahim et al., 2025), and wastewater streams containing heavy metals and organic pollutants (Abu Amr et al., 2023; Rawat et al., 2023). These by-products are typically managed as separate waste streams rather than as recoverable raw materials, leading to a segmented treatment strategy and limited consideration of resource recovery at the system level. These practices worsen climate change and waste accumulation, posing serious risks to ecosystems and human health. In particular, Zn^{2+}-containing effluents discharged from galvanizing-related processes can occur as concentrated process streams, in which Zn^{2+}

✉ Corresponding author. E-mail: jeons@postech.ac.kr

Article history: Received 12 June 2026, Revised 1 October 2026, Accepted 15 October 2026, Available online 5 January 2027

© The Author(s) 2027.

concentrations can reach 1000 mg/L or higher at acidic pH 3, depending on the wastewater source and pretreatment history (Bortot Coelho et al., 2021; Thomas et al., 2023). Thus, the US Environmental Protection Agency has set a stringent secondary drinking water limit of 5 mg/L for Zn^{2+}, which emphasizes the need for more effective treatment strategies (Awadeen et al., 2024; Oladimeji et al., 2024).

Conventional wastewater treatment methods, including activated carbon adsorption (Karnib et al., 2014), membrane separation (Abdullah et al., 2019), and pH-induced precipitation (Kurniawan et al., 2006), have been widely explored. However, their practical implementation is limited by membrane fouling and substantial sludge generation (Park et al., 2019; Chai et al., 2021; Qasem et al., 2021; Raji et al., 2023). Recent studies have investigated engineered adsorbents with high Zn^{2+} removal capacities, such as ferrite nanoparticles (Rafie et al., 2024), chitosan-based nanocomposites (Alhalili and Abdelrahman, 2024), and lignocellulose-based polymer gels (An et al., 2021). Among the materials investigated, interest has grown in calcium carbonate ($CaCO_3$) as an abundant, low-cost, and environmentally compatible treatment medium (Fernández Pérez et al., 2022; Wierzba et al., 2022; Jo et al., 2023; Kim et al., 2023). In addition, $CaCO_3$ can be produced directly from steelmaking slag through CO_2 mineralization, allowing the conversion of two major industrial by-products, CO_2 and slag, into value-added materials (Bonenfant et al., 2008). Because steel slag generation corresponds to approximately 15%–20% of crude steel production by mass (Ibrahim et al., 2025), this by-product constitutes a substantial potential Ca source for CO_2 mineralization. Although steel-slag carbonation has been widely investigated for CO_2 sequestration and construction-material production, targeted polymorph control of slag-derived $CaCO_3$ for metal-ion removal remains less explored (Veetil and Hitch, 2020; Baras et al., 2023).

Among the three polymorphs (calcite, aragonite, and vaterite) of $CaCO_3$, vaterite is a particularly attractive material for heavy metal removal because it improves ion exchange and dissolution-precipitation reaction rates due to its high porosity and high solubility (Zhang et al., 2016; Jin et al., 2024). Although zinc carbonate formation during the dissolution of $CaCO_3$ polymorphs has been reported in aqueous systems (Kim et al., 2024), the Zn^{2+} removal behavior of steel-slag-leachate-derived vaterite and its conversion into recoverable zinc-bearing phases have not been fully evaluated. Hydrozincite ($Zn_5(CO_3)_2(OH)_6$) is a particularly relevant product because it not only serves as a stable sink for toxic metals (Lattanzi et al., 2010) and a gas sorbent (Karadas et al., 2011), but also acts as a precursor to porous ZnO-based materials through facile thermal decomposition (Lin et al., 2014).

In this study, we synthesized vaterite via CO_2 mineralization of steel-slag leachate and used it to remove Zn^{2+} ions from aqueous media. The Zn^{2+} removal process was accompanied by an *in situ* transformation of vaterite into hydrozincite. This process is fundamentally distinct from conventional adsorption, as Zn^{2+} removal proceeds through a dissolution-reprecipitation pathway in which vaterite acts as a self-sacrificial and dynamically evolving solid. By coupling CO_2 mineralization with transformation-driven Zn^{2+} removal, the proposed system not only captures dissolved metal ions but also converts them into a stable and recoverable mineral phase. Overall, the proposed route integrates CO_2 mineralization, Zn^{2+} removal, and hydrozincite formation into a potential strategy for resource recovery from steel-related waste streams.

2 Materials and methods

2.1 Materials

Deionized (DI) water (18.3 MΩ cm) was obtained using a reverse osmosis system (Human Corporation, Korea). *L*-arginine, zinc chloride, iron(III) chloride hexahydrate, chromium(III) chloride hexahydrate, manganese(II) chloride tetrahydrate, ethanol, and ninhydrin were purchased from Sigma-Aldrich (MO, USA). *L*-lysine monohydrochloride, sodium hydroxide, hydrochloric acid, zinc oxide and phenol were obtained from Samchun Chemical (Seoul, Korea). High-purity carbon dioxide (99.9% CO_2) and nitrogen gases (99.9% N_2) were provided by Shinan Gas (Pohang, Korea). Steelmaking slag was obtained from steelworks.

2.2 Preparation of $CaCO_3$ polymorphs by CO_2 mineralization of steel-slag leachate

A 10 wt% slag slurry was prepared by dispersing 25 g of 50–300 μm steel slag powder in 225 mL of DI water and stirring at 300 r/min for 2 h at room temperature. After sedimentation, the suspension was filtered through a 1 μm membrane to obtain the leachate. The crystalline phase compositions of the raw and leached slag were determined by Rietveld refinement of their X-ray diffraction (XRD, Ultima IV, Rigaku) patterns (Figs. S1(a) and S1(b) in the Supplementary material)

and are summarized in Table 1. The dependence of the dissolved Ca^{2+} concentration on slag loading was also examined (Fig. S1(c) in the Supplementary material). Inductively coupled plasma optical emission spectrometry (ICP-OES, SPECTRO, ARCOS FHM22) showed that the resulting leachate contained 16.5 mM Ca^{2+}, with only trace levels of Na^{+}, K^{+}, and Mg^{2+} (Table S1 in the Supplementary material). This leachate was used as the Ca^{2+} source for all subsequent calcite and vaterite syntheses.

CO_2 mineralization experiments were conducted by bubbling CO_2 into steel-slag leachate in the presence of *L*-lysine or *L*-arginine as crystallization modifiers. To examine the effects of mineralization conditions on vaterite formation, screening experiments were performed using *L*-arginine. The *L*-arginine-to-Ca^{2+} molar ratios of 1, 2, 3, and 4 were denoted as R1–R4, respectively. The CO_2 injection rate was varied from 0.5 to 3.0 mL/min, and the solution pH was varied from 8.0 to 10.0.

For $CaCO_3$ synthesis, 50 mL of slag leachate (16.5 mmol/L Ca^{2+}) was placed in a 100 mL beaker, and the amino acid concentration was set at 49.5 mmol/L, corresponding to an amino acid-to-Ca^{2+} molar ratio of 3.0. The pH was maintained at 9.0 throughout the reaction using approximately 1.8 mL of 1 mol/L NaOH and 1.0 mL of 1 mol/L HCl per batch. CO_2 was introduced into the leachate at a flow rate of 1 mL/min for 20 min, and the reaction was conducted at room temperature under stirring at 300 r/min. After the reaction, the suspension was centrifuged at 3000 r/min. The recovered solids were washed with DI water, rinsed with ethanol, and dried in an oven at 60 °C for 5 h. The $CaCO_3$ yield was calculated from the recovered dry mass relative to the theoretical $CaCO_3$ mass based on the initial dissolved Ca^{2+} content. The amount of CO_2 incorporated into the recovered $CaCO_3$ was calculated using the molar mass ratio of CO_2 to $CaCO_3$, and the supplied CO_2 amount was calculated from the gas flow rate and injection time. The CO_2 mineralization efficiency was calculated as the ratio of the incorporated CO_2 amount to the supplied CO_2 amount. For the reuse experiments, the solution recovered by solid–liquid separation after each synthesis cycle was directly reused for the subsequent cycle. The synthesis volume was also increased from 50 to 1000 mL to examine the scalability of vaterite synthesis.

The vaterite content in the recovered solids was calculated using XRD intensity-ratio method (Kontoyannis and Vagenas, 2000). The phase composition, morphology, elemental distribution, functional groups, and specific surface areas of the synthesized particles were characterized by XRD, scanning electron microscopy coupled with energy-dispersive X-ray spectroscopy (SEM-EDS, JEOL, JSM-7800F PRIME), Fourier-transform infrared spectroscopy (FT-IR, FT/IR-4600, JASCO), and N_2 adsorption-desorption analysis using the Brunauer-Emmett-Teller (BET) method (BELSORP-MAX X, MicrotracBEL), respectively.

2.3 Zn^{2+} removal performance of calcite and vaterite

Zn^{2+} removal experiments were conducted by adding 20 mg of calcite or vaterite to 40 mL of an aqueous Zn^{2+} solution at various initial concentrations (100, 300, 500, 700, and 1000 mg/L). The simultaneous processes of Zn^{2+} removal and Ca^{2+} release induced an *in situ* transformation of $CaCO_3$ into hydrozincite. The suspension was stirred at room temperature for 2 h. Then, the suspension was separated, and the supernatant was analyzed by ICP-OES to calculate the Zn^{2+} removal efficiency based on the residual Zn^{2+} concentration. The recovered solids were characterized using XRD, FT-IR, SEM, and EDS.

Time-dependent Zn^{2+} removal by calcite and vaterite was evaluated at an initial Zn^{2+} concentration of 100 mg/L. Dissolved Zn^{2+} and Ca^{2+} concentrations were also monitored during the reaction of vaterite with a 300 mg/L Zn^{2+} solution to examine the relationship between Zn^{2+} removal and mineral transformation. In

Table 1 Crystalline phase compositions of raw and leached steel slag determined by Rietveld refinement

Crystalline phase	Chemical formula	Raw slag (wt%)	Leached slag (wt%)
Portlandite	$Ca(OH)_2$	25.2	1.2
Calcite	$CaCO_3$	11.6	5.3
Larnite	Ca_2SiO_4	22.7	51.9
Brownmillerite	$Ca_2Fe_2O_5$	19.0	26.7
Wüstite	FeO	11.2	9.8
Quartz	SiO_2	10.3	5.1
Total	–	100.0	100.0

addition, the effect of the initial solution pH (3–6) on Zn^{2+} removal by vaterite was examined.

The applicability of vaterite was further evaluated using a synthetic wastewater as a model matrix representing Zn-rich galvanic effluents. A solution containing 1000 mg/L Zn^{2+} and 10 mg/L each of Fe^{3+}, Cr^{3+}, and Mn^{2+} was prepared, and its initial pH was adjusted to 3.0. The Zn^{2+} concentration and initial pH were selected with reference to the concentrated and acidic characteristics of reported galvanic wastewater (Deval et al., 2012; Öztel et al., 2020; Bian et al., 2022; Thomas et al., 2023). Removal experiments were conducted by adding 80 mg of vaterite to 40 mL of the synthetic wastewater and stirring at room temperature for 120 min. After solid–liquid separation, the residual concentrations of Zn, Fe, Cr, and Mn were measured by ICP-OES to determine their removal efficiencies. The recovered solids were characterized using XRD, SEM, and EDS. To evaluate Zn retention in the recovered solids, the hydrozincite obtained after Zn^{2+} removal was subjected to leaching tests in aqueous solutions with initial pH values of 4–8, and the leached Zn concentration was measured by ICP-OES. The overall experimental procedure, from slag leaching and CO_2 mineralization to Zn^{2+} removal and hydrozincite formation, is summarized in Scheme 1. All quantitative experiments were independently repeated three times, and the results are presented as mean ± standard deviation ($n = 3$) with error bars.

3 Results and discussion

3.1 CO_2 mineralization into calcite and vaterite

To establish mineralization conditions suitable for vaterite formation, the effects of CO_2 injection rate and solution pH were first examined using *L*-arginine as a crystallization modifier. As shown in Fig. 1(a), the vaterite content was maximized at a CO_2 flow rate of 1 mL/min, whereas both lower and higher CO_2 flow rates reduced the vaterite fraction. This trend indicates that vaterite formation requires an appropriate CO_2 supply, because the CO_2 flow rate affects dissolved carbonate generation and $CaCO_3$ supersaturation (Sun et al., 2017; Konopacka-Łyskawa et al., 2019). The pH screening results (Fig. 1(b)) showed that high vaterite contents were obtained at pH 8.0–9.0, with pH 9.0 giving the most consistently high vaterite fraction across the tested *L*-arginine loading conditions. This pH range likely provides a favorable supersaturation window for continuous vaterite nucleation while suppressing its recrystallization into calcite (Njegić-Džakula et al., 2010; Hanifa et al., 2025). Based on these results, subsequent $CaCO_3$ syntheses were performed at pH 9.0 and a CO_2 flow rate of 1 mL/min.



Scheme 1 Schematic illustration of the experimental workflow for the integrated CO_2 mineralization of steel-slag leachate and Zn^{2+} removal with hydrozincite formation.

Under these mineralization conditions, Figures 1(c) and 1(d) show the SEM images and corresponding EDS elemental maps of the $CaCO_3$ particles synthesized in the presence of *L*-arginine and *L*-lysine, respectively. The addition of *L*-arginine primarily generated spherical vaterite particles with an average particle size of approximately 1.7 μm (Fig. S2(a)), whereas the addition of *L*-lysine generated well-defined faceted polyhedral crystals with smooth surfaces and an average particle size of approximately 2.0 μm (Fig. S2(b)). The observed morphological differences were consistent with the XRD and FT-IR results. As shown in the XRD patterns (Fig. 1(e)), the sample prepared in the presence of *L*-arginine exhibited characteristic diffraction peaks of vaterite at 24.9° (100), 27.1° (101), and 43.8° (110) (Song et al., 2023). According to the XRD intensity ratio calibration method (Kontoyannis and Vagenas, 2000), the vaterite content was calculated to exceed 99%. In contrast, the sample prepared with *L*-lysine exhibited a dominant (104) peak at 29.4° (Luo et al., 2020), confirming that it was mainly composed of calcite. In the FT-IR spectra (Fig. 1(f)), characteristic vaterite bands at 746 and 1080 cm^{-1} were evident for the arginine-modified sample, whereas the lysine-modified sample showed the calcite band at 712 cm^{-1} (Min et al., 2024). In addition, the BET specific surface area of vaterite was 11.19 m^2/g (Fig. S3(a)), which was approximately 5.7 times higher than that of calcite (1.95 m^2/g; Fig. S3(b)). This higher surface area indicates that the vaterite particles provide more accessible surface sites than the calcite particles.

The amino acid-dependent phase selectivity observed during $CaCO_3$ crystallization arises from differences in

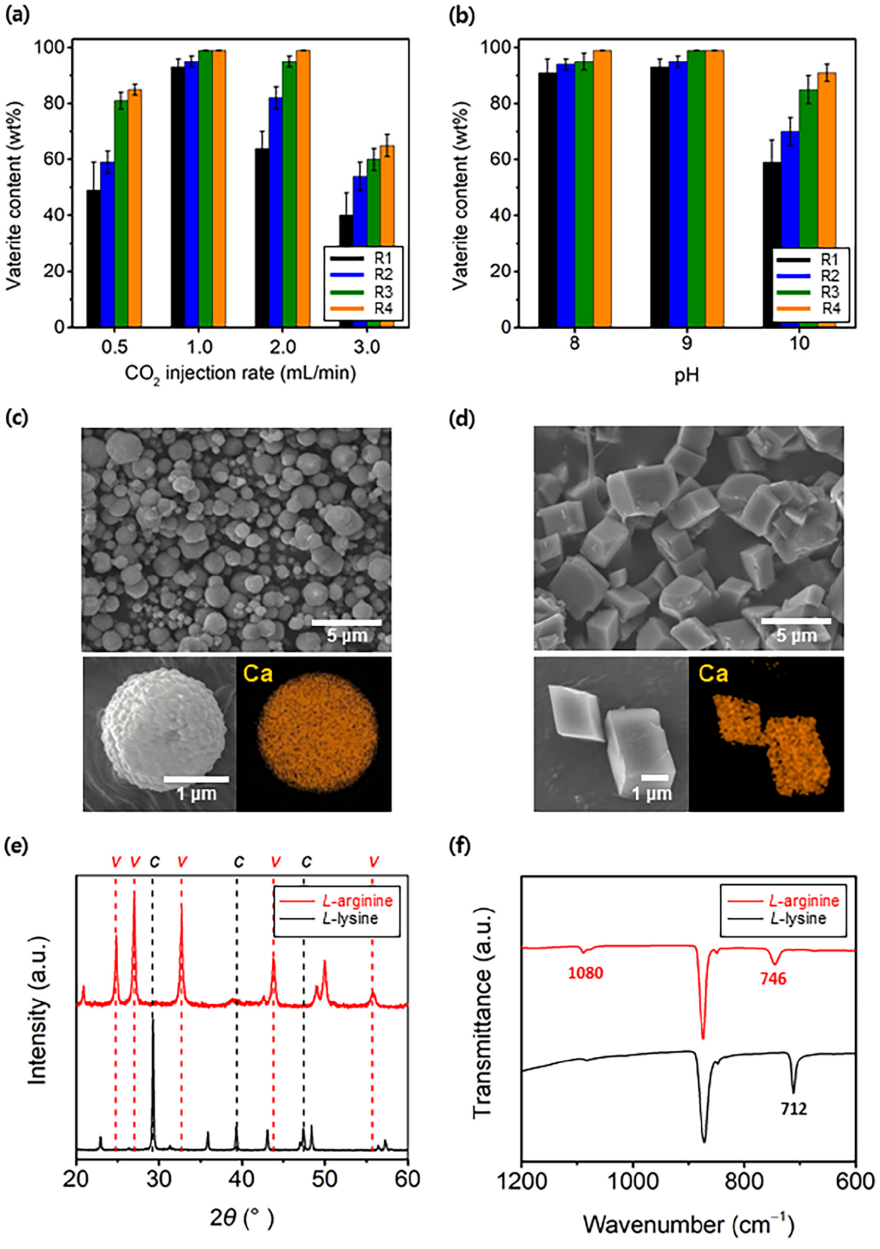


Fig. 1 (a) Effect of CO_2 injection rate and (b) effect of solution pH on the vaterite content during CO_2 mineralization of steel-slag leachate in the presence of *L*-arginine. SEM images and corresponding EDS elemental map of the $CaCO_3$ particles synthesized in the presence of (c) *L*-arginine and (d) *L*-lysine. (e) XRD patterns of the synthesized particles, where *v* and *c* denote the vaterite and calcite phases, respectively; and (f) FT-IR spectra of the same particles.

how amino acids interact with ionic species and crystal growth sites in the early stages of nucleation and growth. *L*-lysine selectively stabilizes calcite through adsorption at active growth sites. This adsorption involves the primary amine group ($–NH_3^+$), which interacts strongly with surface carbonate groups, thereby suppressing step propagation and reinforcing calcite dominance during crystal growth (Jalab et al., 2021; Nahi et al., 2022). In contrast, *L*-arginine strongly interacts with bicarbonate and carbonate species (HCO_3^-/CO_3^{2-}) in solution because of its positively charged guanidinium side chain, thereby perturbing the prenucleation and nucleation pathways and favoring vaterite formation (Guo et al., 2013; Madhav et al., 2023). These interactions increase the nucleation density and distribute growth precursors over a large number of nuclei, resulting in more uniform vaterite particles.

The CO_2 mineralization performance was further quantified under the optimized conditions. The $CaCO_3$ yield was approximately 90%, and the CO_2 mineralization efficiency reached 90.8%, corresponding to a CO_2 fixation of 5.9 mg CO_2 per g of steel slag at the $CaCO_3$ mineralization stage. The *L*-arginine-containing solution was also reused over four successive cycles (Figs. S4(a) and S4(b)). After four cycles, 87.3% of the initial *L*-arginine remained in the solution (from 48.0 to 41.9 mmol/L), and the vaterite content was maintained at approximately 99%. When the synthesis volume was increased 20-fold from 50 to 1000 mL, the vaterite content remained approximately 99%, while the average particle size increased from approximately 1.7 to 3.0 μm (Fig. S5). These results demonstrate the reusability of the crystallization modifier and the scalability of the vaterite synthesis process.

3.2 Zn^{2+} removal by $CaCO_3$ polymorphs and *in situ* phase transformation into hydrozincite

Figure 2(a) shows the change in Zn^{2+} removal capacity of calcite and vaterite as a function of the initial Zn^{2+} concentration (C_0). The Zn^{2+} removal capacity (q) was calculated as follows,

$$q = \frac{(C_0 - C_e)V}{m}, \quad (1)$$

where C_e is the residual Zn^{2+} concentration after 2 h, V is the solution volume, and m is the mass of $CaCO_3$. For both polymorphs, the removal capacity increased with increasing C_0 and gradually approached a plateau. The concentration-dependent removal data were well described by an empirical Langmuir fit ($R^2 \geqslant 0.990$; Fig. S6 and Table S2). The highest experimentally observed removal capacity of vaterite was 633 mg/g, which was approximately 1.4 times higher than that of calcite (444 mg/g) within the tested concentration range. Since the two polymorphs exhibited similar particle sizes, the higher Zn^{2+} removal capacity of vaterite can be attributed to the combined effects of its larger BET specific surface area, higher solubility, and metastable polymorphic nature, which improve surface accessibility and interfacial reactivity toward Zn^{2+} ions. The Zn^{2+} removal capacity of vaterite was comparable to or higher than those of recently reported porous vaterite microspheres and engineered Zn^{2+} adsorbents (Table S3). Moreover, unlike these materials, the present system integrates the synthesis of vaterite from steel-slag leachate with Zn^{2+} removal and hydrozincite recovery.

Figure 2(b) shows the time-dependent Zn^{2+} removal efficiency at initial concentration (C_0) of 100 mg/L. The Zn^{2+} removal efficiency (η) was calculated as follows,

$$\eta = \frac{C_0 - C_t}{C_0} \times 100\%, \quad (2)$$

where C_t is the Zn^{2+} concentration at time t. Upon addition of vaterite particles, η rapidly increased, exceeding 99% within 60 min, whereas a slower increase in η was observed for calcite particles over the same time period. The rapid Zn^{2+} removal of vaterite is due to its relatively large accessible surface area and higher solubility product constant (K_{sp}) (Jin et al., 2024). The time-dependent Zn^{2+} removal data were further described using an empirical pseudo-first-order model (Table S2), and the apparent rate constant (k_1) of vaterite (0.049 min^{-1}) was approximately 2.2 times higher than that of calcite (0.022 min^{-1}). In addition, vaterite achieved high Zn^{2+} removal efficiencies within 120 min over the initial pH range of 3–6 (Fig. S7).

The applicability of vaterite was further examined using a synthetic wastewater containing 1000 mg/L Zn^{2+} and 10 mg/L each of Fe^{3+}, Cr^{3+}, and Mn^{2+} at an

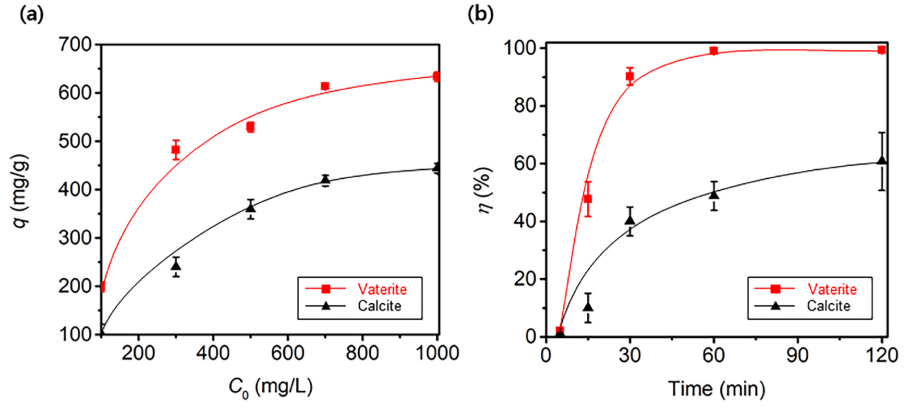


Fig. 2 (a) Zn^{2+} removal capacity (q) of calcite and vaterite as a function of the initial Zn^{2+} concentration. (b) Time-dependent Zn^{2+} removal efficiency of calcite and vaterite at an initial Zn^{2+} concentration of 100 mg/L.

initial pH of 3.0 (Fig. S8). At a vaterite loading of 2.0 g/L, the residual Zn^{2+} concentration decreased to ⩽ 1 mg/L after 120 min, corresponding to a removal efficiency of ⩾ 99.9% (Fig. S8(a)). This concentration was below the U.S. metal-finishing effluent limits for total Zn of 2.61 mg/L (daily maximum) and 1.48 mg/L (monthly average) (U.S. Environmental Protection Agency, 2024). XRD analysis identified hydrozincite together with residual vaterite in the recovered solids, and EDS mapping showed clear Ca and Zn signals (Figs. S8(b) and S8(c)). These results demonstrate that vaterite effectively removes Zn^{2+} through hydrozincite formation even in the presence of co-existing metal ions under acidic conditions.

Figures 3(a) and 3(b) show the XRD patterns and FT-IR spectra of the $CaCO_3$ samples recovered after Zn^{2+} removal, respectively. The results indicate that the Zn^{2+} removal process is accompanied by a crystallographic phase transformation. In the XRD patterns, the vaterite-derived sample showed a pronounced attenuation of the characteristic $CaCO_3$ peaks at 24.9° (100), 27.1° (101), and 43.8° (110), accompanied by the emergence of additional peaks at approximately 28.0° (020), 35.7° (510), and 59.5° (023), consistent with the formation of hydrozincite ($Zn_5(CO_3)_2(OH)_6$) (Nistor et al., 2013). In contrast, the calcite-derived sample exhibited only weak hydrozincite-related features, whereas the intense calcite (104) peak at 29.4° remained dominant, indicating a substantially lower extent of transformation. The corresponding FT-IR spectra further support this observation. For the vaterite-derived sample, a broad O–H stretching band was observed near 3300 cm^{-1}, accompanied by the development of pronounced carbonate-related bands at 1515 and 1383 cm^{-1}, which are attributable to the OH and CO_3^{2-} groups in hydrozincite (Sanna et al., 2013). In contrast, the calcite-derived sample maintained most of the calcite characteristic carbonate bands, including features near 712 and 848 cm^{-1} (Min et al., 2024).

These differences in phase evolution are also reflected in the SEM images and the corresponding EDS elemental maps. Figure 3(c) shows that the vaterite-derived particles underwent extensive structural reorganization when exposed to Zn^{2+}-containing solutions, resulting in nanoflower-like assemblies composed of thin nanosheets radiating from the particle center. The corresponding EDS maps revealed that Zn was the dominant element, with only a small amount of Ca, indicating that a substantial conversion to hydrozincite-rich products occurred. This is consistent

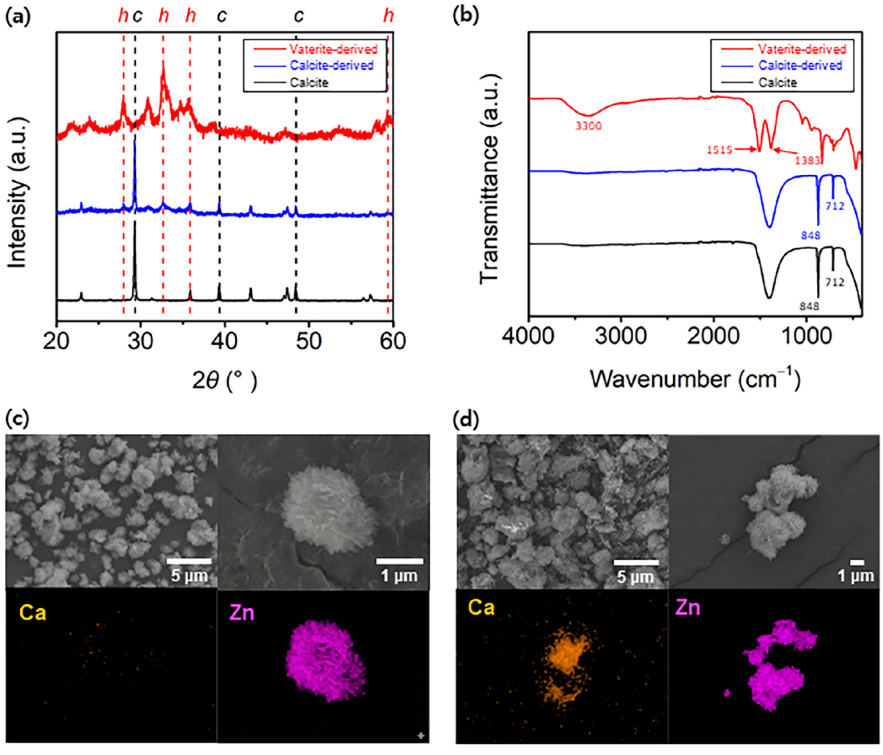


Fig. 3 (a) XRD patterns and (b) FT-IR spectra of the vaterite- and calcite-derived particles; *h* and *c* denote the hydrozincite and calcite phases, respectively. SEM images and corresponding EDS elemental maps of the vaterite-derived (c) and calcite-derived (d) particles.

with the reported growth mechanism, where Zn carbonate (hydrozincite) precipitation on dissolving $CaCO_3$ is governed by the interfacial balance between dissolution and reprecipitation (Martin Soladana, 2017; Kim et al., 2024). In contrast, the limited morphological changes of the calcite-derived particles (Fig. 3(d)) were characterized by the coexistence of Ca and Zn signals, consistent with the formation of Zn-bearing surface precipitates on a largely intact calcite core.

Figure 4 shows the time-dependent changes in the solid phases, solution chemistry, and particle morphology during Zn^{2+} removal by vaterite. As the reaction proceeded, the characteristic vaterite peaks gradually weakened, whereas hydrozincite peaks emerged after 30 min and became more pronounced thereafter, confirming the progressive phase conversion of vaterite into hydrozincite (Fig. 4(a)). At an initial Zn^{2+} concentration of 300 mg/L, the dissolved Zn^{2+} concentration decreased while the Ca^{2+} concentration increased (Fig. 4(b)), indicating that Zn^{2+} removal occurred concurrently with $CaCO_3$ dissolution. The SEM images show a corresponding morphological evolution (Fig. 4(c)), where the initially smooth spherical particles become progressively roughened, followed by the development of nanosheet-like features and the eventual formation of well-developed nanoflower-like assemblies after 120 min. This synchronized phase and morphological evolution provides direct evidence that Zn^{2+} removal is governed by a dissolution-reprecipitation mechanism, wherein metastable vaterite acts as a reactive precursor that is gradually consumed while hydrozincite is formed. The leaching behavior of the recovered hydrozincite was evaluated at initial pH values of 4–8 (Fig. S9). Zn leaching decreased from 8.4% to 0.2% as the initial pH increased from 4 to 8 and remained below 1.4% at pH 6–8, indicating stable Zn retention in the recovered hydrozincite.

3.3 Conversion of hydrozincite into nanoflower-like ZnO

To further highlight the value-added potential of hydrozincite, the recovered particles were thermally converted into nanostructured ZnO, demonstrating its utility as a versatile precursor for zinc-based materials. The hydrozincite particles recovered after the Zn^{2+} removal step were calcined in an N_2 atmosphere at 300

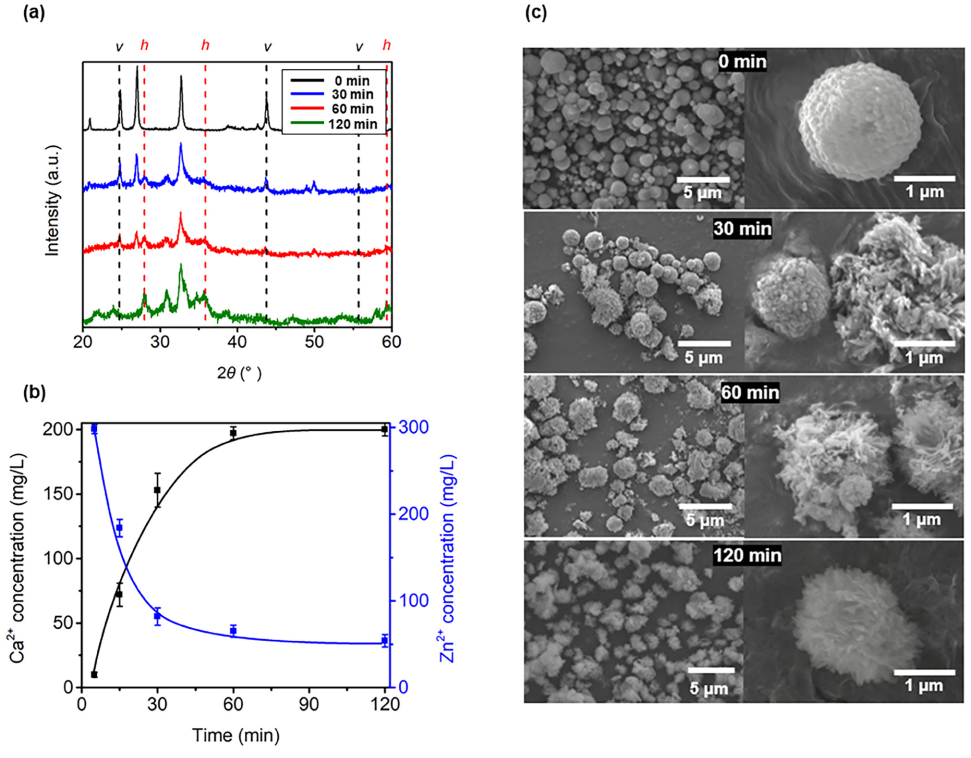


Fig. 4 Time-dependent transformation of vaterite into hydrozincite at an initial Zn^{2+} concentration of 300 mg/L. (a) XRD patterns of the recovered solids at different reaction times. (b) Changes in dissolved Zn^{2+} and Ca^{2+} concentrations during the reaction. (c) SEM images of the solids after 0, 30, 60, and 120 min of reaction.

°C for 3 h to obtain ZnO, following previously reported conditions for hydrozincite-derived ZnO (Moezzi et al., 2014; Kim et al., 2025; Kouchenani and Rezaei, 2026). The ZnO yield was approximately 90% relative to the theoretical ZnO mass calculated from the hydrozincite precursor. Figures 5(a) and 5(b) show the XRD pattern and FT-IR spectrum of the calcined product, respectively. The XRD pattern exhibited well-defined diffraction peaks at 31.7° (100), 34.4° (002), and 36.2° (101) (Wang et al., 2023), whereas the FT-IR spectrum showed characteristic Zn-O stretching bands in the 400-600 cm^{-1} region (Valle et al., 2021), suggesting the formation of predominantly wurtzite ZnO within the detection limit of XRD and FT-IR.

Figure 5(c) shows the SEM images and corresponding EDS elemental map of the resulting ZnO. The ZnO particles exhibited a well-developed nanoflower-like architecture composed of radially assembled nanosheets, whereas the overall particle outline of the hydrozincite precursor was largely retained. This structural preservation indicates that the morphology of the hydrozincite precursor can be effectively transferred to the resulting ZnO through controlled thermal decomposition. EDS mapping confirmed that Zn was homogeneously distributed throughout the entire nanoflower-like ZnO particle. In addition, the BET surface area of 107.8 m^2/g (Fig. S10) indicates that numerous accessible surface sites are exposed over the nanoflower-like framework. To further assess its potential functional utility, the photocatalytic activity of the resulting ZnO was preliminarily evaluated (Fig. S11). Under identical conditions, the C/C_0 of phenol decreased to approximately 0.21 after 150 min of irradiation for the hydrozincite-derived ZnO, compared with approximately 0.65 for commercial ZnO, indicating its higher photocatalytic activity. These results demonstrate that the spent hydrozincite can be upcycled into structurally well-defined ZnO, providing an additional pathway for resource recovery and value enhancement beyond Zn^{2+} removal.

4 Conclusions

In this study, we developed an integrated route that valorizes CO_2, steel slag, and Zn^{2+}-containing wastewater. By combining amino acid-directed crystallization with the CO_2 mineralization of steel-slag leachate, vaterite and calcite, two polymorphs of $CaCO_3$, were selectively synthesized. Under the optimized mineralization conditions, the CO_2 minera-

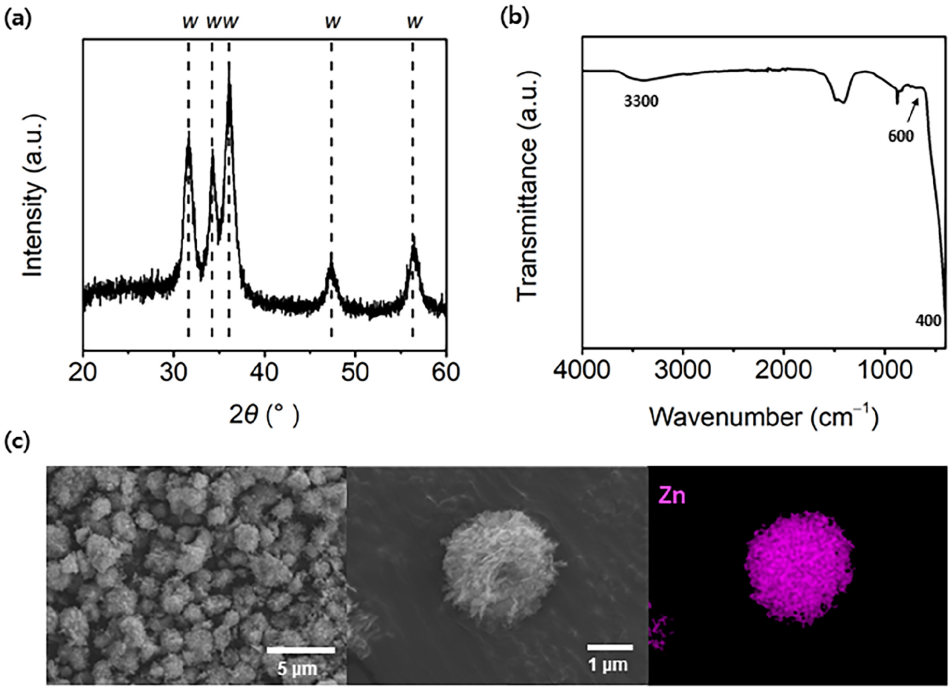


Fig. 5 (a) XRD pattern of ZnO derived from the spent hydrozincite, where *w* denotes the wurtzite phase. (b) FT-IR spectrum of the same sample, confirming the formation of wurtzite ZnO. (c) SEM images and corresponding Zn EDS elemental map of the resulting nanoflower-like ZnO.

lization efficiency reached 90.8%, corresponding to 5.9 mg CO_2 per g of steel slag. The porous and metastable vaterite exhibited superior Zn^{2+} removal performance compared to calcite, with the highest observed removal capacity of 633 mg/g and a removal efficiency exceeding 99% within 60 min. This difference was associated with the larger BET specific surface area of vaterite (11.19 m^2/g) compared with calcite (1.95 m^2/g), as well as its metastable nature and relatively high solubility. During Zn^{2+} removal, vaterite underwent a progressive phase transformation into Zn-rich hydrozincite through a dissolution-reprecipitation pathway, whereas calcite showed only limited conversion. Time-dependent XRD and SEM analyses consistently showed the gradual disappearance of vaterite and the formation of nanoflower-like hydrozincite, indicating that the removal process is accompanied by continuous structural and compositional changes. The resulting hydrozincite provides a stable form for Zn retention and can be further converted into ZnO through thermal treatment, with a yield of approximately 90% relative to the theoretical ZnO mass, suggesting a possible route for subsequent utilization of the recovered material. Overall, this study demonstrates that CO_2 mineralization can be effectively combined with Zn^{2+} removal and subsequent material conversion, offering a potential approach for resource recovery and waste minimization in steel-related industrial systems.

CRediT authorship contribution statement

Jaemin Park: Writing-original draft, Visualization, Methodology, Investigation, Conceptualization. **Hyunsoo Han:** Writing-review & editing, Investigation. **Sangmin Jeon:** Writing-review & editing, Supervision, Project administration, Funding acquisition, Conceptualization.

Conflicts of interest The authors declare that they have no known competing financial interests or personal relationships that could have appeared to influence the work reported in this paper.

Acknowledgements This work was supported by Korea Institute of Energy Technology Evaluation and Planning (KETEP) and the Ministry of Climate, Energy & Environment (MCEE) of the Republic of Korea (No. RS-2026-25534493).

Electronic supplementary material Supplementary material is available in the online version of this article at https://dx.doi.org/10.1007/s11783-027-2327-9 and is accessible for authorized users.

Funding note Open Access funding enabled and organized by Pohang University of Science and Technology (POSTECH).

Open access This article is licensed under a Creative Commons Attribution 4.0 International License, which permits use, sharing, adaptation, distribution and reproduction in any medium or format, as long as you give appropriate credit to the original author(s) and the source, provide a link to the Creative Commons licence, and indicate if changes were made. The images or other third party material in this article are included in the article's Creative Commons licence, unless indicated otherwise in a credit line to the material. If material is not included in the article's Creative Commons licence and your intended use is not permitted by statutory regulation or exceeds the permitted use, you will need to obtain permission directly from the copyright holder. To view a copy of this licence, visit http://creativecommons.org/licenses/by/4.0/.

References

Abdullah N, Yusof N, Lau W J, Jaafar J, Ismail A F (2019). Recent trends of heavy metal removal from water/wastewater by membrane technologies. Journal of Industrial and Engineering Chemistry, 76: 17–38

Abu Amr S S, Abujazar M S S, Karaağaç S U, Mehdi K K, Alazaiza M Y D, Bashir M J K, Fatihah S, Vakili A H (2023). Factorial design and optimization of date stone as a natural coagulant for organic and heavy metals removal from industrial wastewater. Global NEST Journal, 25(1): 99–107

Alhalili Z, Abdelrahman E A (2024). Efficient removal of Zn(II) ions from aqueous media using a facilely synthesized nanocomposite based on chitosan Schiff base. Scientific Reports, 14(1): 17598

An Y H, Zhang W Q, Liu H, Zhong Y, Hu Z C, Shao Y L, Chen Z J, Ren Y K, Wang B Y, Wang S, et al. (2021). Lignocellulose-based superabsorbent polymer gel crosslinked with magnesium aluminum silicate for highly removal of Zn (II) from aqueous solution. Polymers, 13(23): 4161

Awadeen N A, Eltarahony M, Zaki S, Yousef A, El-Assar S, El-Shall H (2024). Fungal carbonatogenesis process mediates zinc and chromium removal via statistically optimized carbonic anhydrase enzyme. Microbial Cell Factories, 23(1): 236

Baras A, Li J J, Ni W, Hussain Z, Hitch M (2023). Evaluation of potential factors affecting steel slag carbonation. Processes, 11(9): 2590

Bian R, Su T, Gao Y D, Chen Y, Zhu S Y, Liu C G, Wang X Z, Qu Z, Zhang Y X, Zhang H (2022). Enrichment and recycling of Zn from electroplating wastewater as zinc phosphate via coupled coagulation and hydrothermal route. Arabian Journal of Chemistry, 15: 103664

Bonenfant D, Kharoune L, Sauvé S, Hausler R, Niquette P, Mimeault M, Kharoune M (2008). CO_2 sequestration potential of steel slags at ambient pressure and temperature. Industrial & Engineering Chemistry Research, 47(20): 7610–7616

Bortot Coelho F E, Oliveira V S, Araújo E M R, Balarini J C, Konzen C, Salum A, Miranda T L S (2021). Treatment of a wastewater from a galvanizing industry containing chromium(VI) and zinc(II) by liquid surfactant membranes technique. Journal of Environmental Science and Health, Part A, 56(3): 289–302

Chai W S, Cheun J Y, Kumar P S, Mubashir M, Majeed Z, Banat F,

Ho S H, Show P L (2021). A review on conventional and novel materials towards heavy metal adsorption in wastewater treatment application. Journal of Cleaner Production, 296: 126589

Deval C G, Mane A V, Joshi N P, Saratale G D (2012). Phyto-remediation potential of aquatic macrophyte Azolla caroliniana with references to zinc plating effluent. Emirates Journal of Food and Agriculture, 24(3): 208–223

Fernández Pérez B, Ayala Espina J, de Los Ángeles Fernández González M (2022). Adsorption of heavy metals ions from mining metallurgical tailings leachate using a shell-based adsorbent: characterization, kinetics and isotherm studies. Materials, 15(15): 5315

Guo Y M, Wang F F, Zhang J, Yang L, Shi X M, Fang Q L, Ma X M (2013). Biomimetic synthesis of calcium carbonate with different morphologies under the direction of different amino acids. Research on Chemical Intermediates, 39(6): 2407–2415

Hanifa M, Sharma U, Thapliyal P C, Singh L P (2025). Effects of temperature, pH and calcium-to-carbonate ratio on the calcium carbonate polymorphs. Discover Civil Engineering, 2(1): 147

Ibrahim I K, Rady M, Tawfik N M, Kassem M, Mahfouz S Y (2025). Enhancing strength and sustainability of concrete with steel slag aggregate. Scientific Reports, 15(1): 17068

Jalab R, Saad M A, Hussein I A, Onawole A T (2021). Calcite scale inhibition using environmental-friendly amino acid inhibitors: DFT investigation. ACS Omega, 6(47): 32120–32132

Jin B B, Wang S, Lei Y Z, Jia H, Niu Q, Dapaah M F, Gao Y, Cheng L (2024). Green and effective remediation of heavy metals contaminated water using $CaCO_3$ vaterite synthesized through biomineralization. Journal of Environmental Management, 353: 120136

Jo Y H, Jeong W G, Park J, Baek K (2023). Partially calcined $CaCO_3$ for remediating multi-heavy metals-contaminated groundwater. Chemical Engineering Journal, 471: 144652

Karadas F, Yavuz C T, Zulfiqar S, Aparicio S, Stucky G D, Atilhan M (2011). CO_2 adsorption studies on hydroxy metal carbonates $M(CO_3)_x(OH)_y$ (M = Zn, Zn–Mg, Mg, Mg–Cu, Cu, Ni, and Pb) at high pressures up to 175 bar. Langmuir, 27(17): 10642–10647

Karnib M, Kabbani A, Holail H, Olama Z (2014). Heavy metals removal using activated carbon, silica and silica activated carbon composite. Energy Procedia, 50: 113–120

Kim J, Sovacool B K, Bazilian M, Griffiths S, Lee J, Yang M, Lee J (2022). Decarbonizing the iron and steel industry: a systematic review of sociotechnical systems, technological innovations, and policy options. Energy Research & Social Science, 89: 102565

Kim J J, Lee S S, Fenter P, Myneni S C B, Nikitin V, Peters C A (2023). Carbonate coprecipitation for Cd and Zn treatment and evaluation of heavy metal stability under acidic conditions. Environmental Science & Technology, 57(8): 3104–3113

Kim M Y, Choa H, Park C O, To D T H, Cao T K P, Mendoza E R, Jin C, Lee B Z, Myung N V, Lee K H (2025). Boundary engineering of porous zinc oxide nanosheets to enhance gas sensing performance. Sensors and Actuators Reports, 9: 100322

Kim Y, Lee S S, Abdilla B, Nikitin V, Sturchio N C, Fenter P (2024). Formation of zinc carbonate phases on dissolving calcite, aragonite, and vaterite in acidic aqueous solutions. Geochimica et Cosmochimica Acta, 380: 131–139

Konopacka-Łyskawa D, Kościelska B, Łapiński M (2019). Precipitation of spherical vaterite particles via carbonation route in the bubble column and the gas-lift reactor. JOM, 71(3): 1041–1048

Kontoyannis C G, Vagenas N V (2000). Calcium carbonate phase analysis using XRD and FT-Raman spectroscopy. Analyst, 125(2): 251–255

Kouchenani G, Rezaei M (2026). Statistical optimization of high specific surface area zinc oxide synthesized through carbonation and thermal decomposition using response surface methodology. Scientific Reports, 16(1): 10471

Kurniawan T A, Chan G Y S, Lo W H, Babel S (2006). Physico–chemical treatment techniques for wastewater laden with heavy metals. Chemical Engineering Journal, 118(1−2): 83–98

Lattanzi P, Meneghini C, De Giudici G, Podda F (2010). Uptake of Pb by hydrozincite, $Zn_5(CO_3)_2(OH)_6$: implications for remediation. Journal of Hazardous Materials, 177(1−3): 1138–1144

Lin Z D, Guo F, Wang C, Wang X H, Wang K, Qu Y (2014). Preparation and sensing properties of hierarchical 3D assembled porous ZnO from zinc hydroxide carbonate. RSC Advances, 4(10): 5122–5129

Luo X P, Song X W, Cao Y W, Song L, Bu X Z (2020). Investigation of calcium carbonate synthesized by steamed ammonia liquid waste without use of additives. RSC Advances, 10(13): 7976–7986

Madhav D, Coppitters T, Ji Y K, Thielemans W, Desplentere F, Moldenaers P, Vandeginste V (2023). Amino acid promoted single-step carbon dioxide capture and mineralization integrated with polymer-mediated crystallization of carbonates. Journal of Cleaner Production, 415: 137845

Martin Soladana P M (2017). Characterization and modeling of hydrozincite precipitation in continuous tubular reactor. A study on nucleation and aggregation. Dissertation for Doctoral Degree. Leeds: University of Leeds

Min K H, Kim D H, Pack S P (2024). Size control of biomimetic curved-edge vaterite with chiral toroid morphology via sonochemical synthesis. Biomimetics, 9(3): 174

Moezzi A, Cortie M, Dowd A, McDonagh A (2014). On the formation of nanocrystalline active zinc oxide from zinc hydroxide carbonate. Journal of Nanoparticle Research, 16(4): 2344

Nahi O, Broad A, Kulak A N, Freeman H M, Zhang S H, Turner T D, Roach L, Darkins R, Ford I J, Meldrum F C (2022). Positively charged additives facilitate incorporation in inorganic single crystals. Chemistry of Materials, 34(11): 4910–4923

Nistor L C, Nistor S V, Ghica D (2013). Low temperature tem investigation of electron beam induced decomposition of nanocrystalline hydrozincite into ZnO. Romanian Reports in

Physics, 65(1): 186–192

Njegić-Džakula B, Falini G, Brečević L, Skoko Ž, Kralj D (2010). Effects of initial supersaturation on spontaneous precipitation of calcium carbonate in the presence of charged poly-l-amino acids. Journal of Colloid and Interface Science, 343(2): 553–563

Oladimeji T E, Oyedemi M, Emetere M E, Agboola O, Adeoye J B, Odunlami O A (2024). Review on the impact of heavy metals from industrial wastewater effluent and removal technologies. Heliyon, 10(23): e40370

Öztel M D, Kuleyin A, Akbal F (2020). Treatment of zinc plating wastewater by combination of electrocoagulation and ultra-filtration process. Water Science and Technology, 82(4): 663–672

Park J E, Lee G B, Hong B U, Hwang S Y (2019). Regeneration of activated carbons spent by waste water treatment using KOH chemical activation. Applied Sciences, 9(23): 5132

Qasem N A A, Mohammed R H, Lawal D U (2021). Removal of heavy metal ions from wastewater: a comprehensive and critical review. npj Clean Water, 4(1): 36

Rafie S F, Abu-Zahra N, Sabetvand R (2024). Enhancing Zn (II) recovery efficiency: bi-divalent nickel–cobalt ferrite spinel $Ni_xCo_{1-x}Fe_2O_4$ as a game-changing adsorbent: an experimental and computational study. Chemosphere, 362: 142702

Raji Z, Karim A, Karam A, Khalloufi S (2023). Adsorption of heavy metals: mechanisms, kinetics, and applications of various adsorbents in wastewater remediation: a review. Waste, 1(3): 775–805

Rawat A, Srivastava A, Bhatnagar A, Gupta A K (2023). Technological advancements for the treatment of steel industry wastewater: effluent management and sustainable treatment strategies. Journal of Cleaner Production, 383: 135382

Sanna R, de Giudici G, Scorciapino A M, Floris C, Casu M (2013). Investigation of the hydrozincite structure by infrared and solid-state NMR spectroscopy. American Mineralogist, 98(7): 1219–1226

Song X W, Tuo Y X, Li D, Hua X R, Wang R M, Xue J W, Yang R H, Bu X Z, Luo X P (2023). A green approach to preparing vaterite $CaCO_3$ for clean utilization of steamed ammonia liquid waste and CO_2 mineralization. Sustainability, 15(17): 13275

Sun J, Wang L S, Zhao D F (2017). Polymorph and morphology of $CaCO_3$ in relation to precipitation conditions in a bubbling system. Chinese Journal of Chemical Engineering, 25(9): 1335–1342

Thomas M, Melichová Z, Šuránek M, Kuc J, Więckol-Ryk A, Lochyński P (2023). Removal of zinc from concentrated galvanic wastewater by sodium trithiocarbonate: process optimization and toxicity assessment. Molecules, 28(2): 546

U.S. Environmental Protection Agency (2024). Effluent limitations representing the degree of effluent reduction attainable by applying the best practicable control technology currently available (BPT). Code of Federal Regulations, 40 CFR § 433.13

Valle A L, Silva A C A, Dantas N O, Sabino-Silva R, Melo F C C, Moreira C S, Oliveira G S, Rodrigues L P, Goulart L R (2021). Application of ZnO nanocrystals as a surface-enhancer FTIR for glyphosate detection. Nanomaterials, 11(2): 509

Veetil S P, Hitch M (2020). Recent developments and challenges of aqueous mineral carbonation: a review. International Journal of Environmental Science and Technology, 17(10): 4359–4380

Wang C C, Lo A Y, Cheng M C, Chang Y S, Shih H C, Shieu F S, Tsai H T (2023). Zinc oxide nanostructures enhanced photo-luminescence by carbon-black nanoparticles in Moiré heterostructures. Scientific Reports, 13(1): 9704

Wierzba S, Makuchowska-Fryc J, Kłos A, Ziembik Z, Ochędzan-Siodłak W (2022). Role of calcium carbonate in the process of heavy metal biosorption from solutions: synergy of metal removal mechanisms. Scientific Reports, 12(1): 17668

Zhang J, Yao B, Ping H, Fu Z Y, Li Y, Wang W M, Wang H, Wang Y C, Zhang J Y, Zhang F (2016). Template-free synthesis of hierarchical porous calcium carbonate microspheres for efficient water treatment. RSC Advances, 6(1): 472–480